Available online at www.sciencedirect.com
SCIENCE DIRECT
International Journal of Heat and Fluid Flow 27 (2006) 229–242
International Journal of HEAT AND FLUID FLOW
www.elsevier.com/locate/ijhff

# Computation of unsteady flow and aerodynamic noise of NACA0018 airfoil using large-eddy simulation

H.-J. Kim [a], S. Lee [a,*], N. Fujisawa [b]

[a] Department of Mechanical Engineering, Inha University, 253 Yonghyun-dong, Nam-gu, Incheon 402-751, Korea
[b] Department of Mechanical and Production Engineering, Niigata University, 8050 Ikarashi-2, Niigata 950-2181, Japan

Received 27 July 2004; received in revised form 14 July 2005; accepted 18 August 2005
Available online 25 October 2005

**Abstract**

The flow field around a symmetrical NACA airfoil in the uniform flow under generation of noise was numerically studied. The numerical simulation was carried out by a large-eddy simulation that employs a deductive dynamic model as the subgrid-scale model. The results at small angle of attack $\alpha = 3$–$6°$ indicate that the discrete frequency noise is generated when the separated laminar flow reattaches near the trailing edge of pressure side and the strong instability thereafter affects positive vortices shed near the trailing edge. The quasi-periodic behavior of negative vortex formation on the suction side is affected by the strength and the periodicity of positive vortices near the trailing edge. The computation using aero-acoustic analogy indicates the primary discrete peak at the Strouhal frequency ($=2f \cdot \delta/U_0$) of 0.15 by the vortex shedding from the trailing edge, which is in a close agreement with the experiment.


*Keywords:* Discrete tone noise; LES; Subgrid-scale model; Aero-acoustics

## 1. Introduction

The study of aerodynamic noise from an airfoil in a stream has been an important research topic for the design of a high-performance low-noise turbomachinery. When the airfoil is located in the stream at relatively low Reynolds numbers, a discrete frequency noise is generated from the airfoil inclined at a small angle of attack against the free-stream (Paterson et al., 1973). The basic mechanism of this noise generation was studied by Tam (1974), who suggested that the noise be emitted from the self-excited feedback loop, which consists of large-scale unstable disturbances in the boundary layer and wake flow, and the feedback acoustic waves. However, it has not been confirmed experimentally.

The physical mechanism of noise generation was studied by visualizations and measurements of the flow around airfoil (Akishita, 1986; Hayashi et al., 1995; Fujisawa et al., 2001; Tomimatsu and Fujisawa, 2002). More recently, the mean-flow and turbulence characteristics of the flow around airfoil was investigated by the liquid crystal and PIV measurements (Nakano et al., 2002), which allowed preliminary understanding of the complex behavior of the flow separation and reattachment of boundary layers and the periodic behavior of vortex shedding from the trailing edge of the airfoil, leading to the generation of discrete frequency noise.

The accurate prediction of the flow field around the airfoil over a wide range of flow conditions is very important for the aerodynamic design of a turbomachine. Although significant progress has been made in the viscous flow solution of turbomachinery in the 1980s (Dawes, 1986; Denton, 1986; Hah, 1987), only a few attempts have been made to simulate the unsteady flows of turbomachinery in the spectral sense (Saxer-Felici et al., 2000; Lee et al., 2004a,b). The difficulties related to the simulation, e.g. LES, of unsteady flows around the airfoil are too many to list. One of them is the fine grid resolution which requires that the first grid point adjacent to the blade wall should have an order of

* Corresponding author. Tel.: +82 32 860 7325; fax: +82 32 868 1716.
*E-mail address:* sbaelee@inha.ac.kr (S. Lee).

0142-727X/$ - see front matter © 2005 Elsevier Inc. All rights reserved.
doi:10.1016/j.ijheatfluidflow.2005.08.007

one in the wall unit ($y^+ = u^* y/\nu$). The lack of versatility of models when treating the mixed problem of transition to turbulence, separation, and vortex shedding serves as one of the difficulties.

The low Mach-number self-noise problem of the airfoil is solved efficiently by employing the Lighthill's acoustic analogy. This approach involves an unsteady flow-field prediction from Navier–Stokes equations and an acoustic-field computation by using a free-space acoustic Green's function or a hard-wall Green function for the surface reflection of acoustic waves (Ffowcs Williams and Hall, 1970). In the latter approach of the hard-wall Green's function, a semi-infinite plate with zero thickness was assumed to compute the trailing-edge noise by the turbulent flow over a beveled flat strut (Wang and Moin, 2000). An approximate, three-dimensional, time-harmonic, acoustic Green's function was developed for the sources near the leading or trailing edge (Howe, 2001). Oberai et al. (2000, 2002) considered the problem of scattering effects of the trailing edge of finite-chord NACA0018 and Eppler airfoils by using the variational formulation of Lighthill's acoustic analogy.

The purpose of the present paper is to numerically study the flow over and around the symmetrical airfoil in the uniform flow under the generation of discrete frequency noise. The simulations are conducted to explore the flow behavior near the trailing edge of the airfoil and the radiated noise by the large-eddy simulation and the aero-acoustic analogy. To identify the unsteady structures near the TE of the airfoil, the organized vortex structures and the time–frequency characteristics of unsteady pressures in the boundary layer are analyzed.

## 2. Computational procedure

### 2.1. Deductive dynamic subgrid-scale model in LES

Large-eddy simulation involves the filtering of the equations for continuity and momentum transport. The filtering operation as in Eq. (1), denoted by an overbar and defined as the convolution integral of the field with a filter kernel $G$, substantially reduces the amplitude of the high-frequency spatial Fourier components of any flow variable $F$.

$$\overline{F}(\underline{x}) = \int_D G(\underline{x} - \underline{z}, \Delta) F(\underline{z})\, \mathrm{d}\underline{z} \tag{1}$$

where $\Delta$ is the width or characteristic length scale associated with the filter, and $D$ is the domain of concern. A normalized Gaussian filter in three dimensions is given as an example

$$G(\underline{x} - \underline{z}, \Delta) = \left(\sqrt{\frac{6}{\pi \Delta^2}}\right)^3 \mathrm{e}^{\frac{-6(\underline{x}-\underline{z})^2}{\Delta^2}} \tag{2}$$

The grid-filtered variable can be expanded in terms of Taylor series for the Gaussian filter as

$$\overline{F}(\underline{x}) = \left[1 + \frac{\Delta^2 \nabla^2}{24} + \frac{1}{2!}\left(\frac{\Delta^2 \nabla^2}{24}\right)^2 + \cdots\right] F(\underline{x}) \tag{3}$$

The resulting LES continuity and transport equations are

$$\frac{\partial \bar{u}_i}{\partial x_i} = 0 \tag{4}$$

$$\frac{\partial \bar{u}_i}{\partial t} + \frac{\partial (\bar{u}_i \bar{u}_j)}{\partial x_j} = -\frac{\partial \bar{p}}{\partial x_i} + \nu \nabla^2 \bar{u}_i - \frac{\partial \tau_{ij}}{\partial x_j} \tag{5}$$

where $\tau_{ij} \equiv \left(\overline{\bar{u}_i \bar{u}_j} - \bar{u}_i \bar{u}_j + \overline{u_i' \bar{u}_j} + \overline{\bar{u}_i u_j'} + \overline{u_i' u_j'}\right) = \left(\overline{u_i u_j} - \bar{u}_i \bar{u}_j\right)$ is called the subgrid-scale stress tensor.

Smagorinsky (1963) was the first to propose a model for the subgrid-scale stresses. His model assumes that they follow a gradient-diffusion process, similar to molecular motion. It is still the most popular algebraic eddy viscosity model. The dynamic subgrid-scale turbulence model was proposed by Germano et al. (1991) to simulate closely the state of the flow by locally calculating the eddy viscosity coefficient through double filtering. This model exhibits the proper asymptotic behavior near wall boundaries or in laminar flow without requiring damping or intermittency. However, their model is more demanding from the double filtering at each time step in terms of computation time than the eddy viscosity model.

Applying both grid and test filters, $G$ and $T$, to the continuity and the momentum transport equations yields

$$\frac{\partial \hat{\bar{u}}_i}{\partial x_i} = 0 \tag{6}$$

$$\frac{\partial \hat{\bar{u}}_i}{\partial t} + \frac{\partial (\hat{\bar{u}}_i \hat{\bar{u}}_j)}{\partial x_j} = -\frac{\partial \hat{\bar{p}}}{\partial x_i} + \nu \nabla^2 \hat{\bar{u}}_i - \frac{\partial T_{ij}}{\partial x_j} \tag{7}$$

where the turbulent stress tensor $T_{ij}$ is defined as $\widehat{\overline{u_i u_j}} - \hat{\bar{u}}_i \hat{\bar{u}}_j$. Here the symbol "$\hat{}$" denotes the test filtering operation ($T$) and the symbol "$\bar{}$" denotes the grid filtering operation ($G$). Combining the grid and test-filter GT, the algebraic eddy viscosity model, $T_{ij}$ can be assumed as

$$T_{ij} = 2C\Delta_{\mathrm{GT}}^2 |\hat{\bar{S}}| \hat{\bar{S}}_{ij} \tag{8}$$

where $\Delta_{\mathrm{GT}}$ is given as $(\Delta_{\mathrm{G}}^2 + \Delta_{\mathrm{T}}^2)^{1/2}$ by Germano (1992).

The resolved turbulent stress tensor, $L_{ij}$, is defined as

$$L_{ij} = T_{ij} - \widehat{\tau_{ij}} = \widehat{\overline{u_i u_j}} - \hat{\bar{u}}_i \hat{\bar{u}}_j \tag{9}$$

where the elements of $L_{ij}$ are resolved components of the stress tensor associated with scales of the motion between the test scale and the grid scale. We can also define $M_{ij}$ as follows:

$$M_{ij} = \left(\Delta_{\mathrm{GT}}^2 |\hat{\bar{S}}| \hat{\bar{S}}_{ij} - \Delta_{\mathrm{G}}^2 \widehat{|\bar{S}| \bar{S}_{ij}}\right) \tag{10}$$

Lilly (1992) suggested that the error in $C$ can be minimized by applying a least-square approach to Germano's dynamic procedure:

$$C(x, y, z, t) = -\frac{1}{2} \frac{L_{ij} M_{ij}}{M_{ij} M_{ij}} \tag{11}$$

If we apply the Taylor series expansion to test-filtered quantities, we have

$$L_{ij} = \frac{\Delta_T^2}{12}\frac{\partial \bar{u}_i}{\partial x_l}\frac{\partial \bar{u}_j}{\partial x_l} - \frac{\Delta_T^4}{24^2}\frac{\partial^2 \bar{u}_i}{\partial x_l^2}\frac{\partial^2 \bar{u}_j}{\partial x_m^2} + \frac{\Delta_T^4}{1152}\left[\frac{\partial^2}{\partial x_l^2}\frac{\partial^2}{\partial x_m^2}\bar{u}_i\bar{u}_j - \left(\bar{u}_i\frac{\partial^2}{\partial x_l^2}\frac{\partial^2}{\partial x_m^2}\bar{u}_j + \bar{u}_j\frac{\partial^2}{\partial x_l^2}\frac{\partial^2}{\partial x_m^2}\bar{u}_i\right)\right] + \cdots \quad (12)$$

$$M_{ij} = \left(\Delta_{GT}^2 - \Delta_G^2\right)\overline{|S|}\bar{S}_{ij} + \frac{\Delta_T^2(\Delta_{GT}^2 - \Delta_G^2)}{24} \times \left(\overline{|S|}\frac{\partial^2 \bar{S}_{ij}}{\partial x_l^2} + \bar{S}_{ij}\frac{\partial^2 \overline{|S|}}{\partial x_m^2}\right) + \Delta_{GT}^2\left(\frac{\Delta_T^2}{24}\right)^2\frac{\partial^2 \overline{|S|}}{\partial x_l^2}\frac{\partial^2 \bar{S}_{ij}}{\partial x_m^2} - \frac{\Delta_G^2\Delta_T^2}{12}\frac{\partial \overline{|S|}}{\partial x_l}\frac{\partial \bar{S}_{ij}}{\partial x_l} + \frac{\Delta_T^4}{1152}\left[\Delta_{GT}^2|\bar{S}|\frac{\partial^2}{\partial x_l^2}\frac{\partial^2}{\partial x_m^2}\bar{S}_{ij} + \Delta_{GT}^2\bar{S}_{ij}\frac{\partial^2}{\partial x_l^2}\frac{\partial^2}{\partial x_m^2}|\bar{S}| - \frac{\partial^2}{\partial x_l^2}\frac{\partial^2}{\partial x_m^2}\Delta_G^2|\bar{S}|\bar{S}_{ij}\right] + \cdots \quad (13)$$

The derivations of $L_{ij}$ and $M_{ij}$ are given in detail in Appendix A. The turbulent eddy viscosity using dynamic Smagorinsky constant is determined as

$$\nu_T = C\Delta_G^2|\bar{S}| \quad (14)$$

The dynamic Smagorinsky constant, $C$, obtained deductively by using Eqs. (11)–(13) is applied to solve the subgrid-scale stress tensor $\tau_{ij}$ in Eq. (5). This deductive dynamic SGS model was tested for the flows of complex geometry without averaging in a homogeneous direction for smoothing which has usually prevented the dynamic model from being applied to the flows in the turbomachinery (Lee et al., 2004a,b).

### 2.2. Numerical method and boundary condition

The numerical simulation of unsteady, turbulent flow around an airfoil was performed with the modified ANSWER code (Runchal and Bhatia, 1993), which accommodates the subgrid-scale model proposed by Lee et al. (2004a) for LES computation.

The governing Navier–Stokes equations are integrated by finite volume method (FVM) for a collocated, structured grid system. A major advantage of this method is that it intrinsically preserves mass and material fluxes both on local and global scales. The numerical integration starts with the assumption of an integration profile for the state variable. The QUICK scheme (Leonard, 1979) was applied to the non-orthogonal grid system in this research. The alternating direction implicit (ADI) solution was used, which solves the set of algebraic equations in three sweeping directions. This temporal discretization of the ADI method is proven to be unconditionally stable in a linear sense. But it may not be accurate in time if the time step is large due to the neglecting of the third-order term that is essential to the factorization.

To capture the physics of vortex formation around the trailing edge and its discrete frequency noise, the cases of $Re_{CL} = 1.6 \times 10^5$ ($U_0 = 30$ m/s, CL (Chord Length) = 80 mm) and attack angles of 0°, 3°, 6°, 9° were numerically simulated by the LES which employs the deductive dynamic model as subgrid-scale model. In the simulation, the flow field is calculated by using an H-type grid system of $296 \times 103 \times 31$ in $x_1$-, $x_2$-, and $x_3$-directions. The spanwise length in the $x_3$-direction is set to be twice the chord length to make sure that it be much greater than the spanwise coherence length (Lee et al., 2004b). The inlet boundary is placed five times chord length (CL) upstream of the leading edge of the blade while the outlet boundary is placed 10CL downstream of the trailing edge of the blade. The grid system and boundary conditions are schematically shown in Fig. 1. The convective boundary condition proposed by Hayder and Turkel (1995) is used to allow the vortical disturbance in the wake to leave the boundary smoothly. Furthermore, the grids are stretched near the computational boundary to diffuse the vortical structures that might cause reflections from the computational domain.

### 2.3. Aero-acoustic computation

A hybrid method using acoustic analogy was employed to compute the far-field sound and directivity patterns

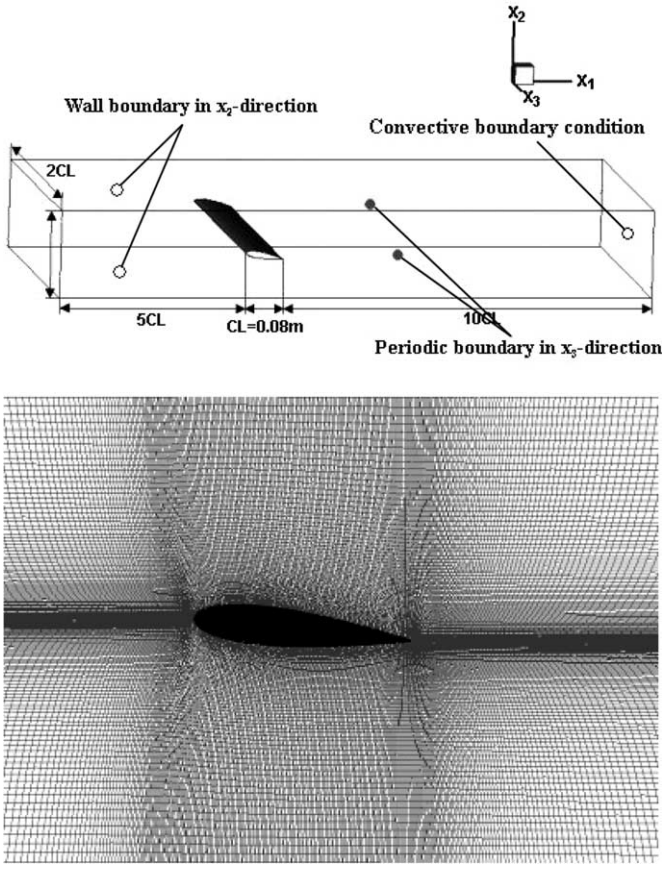


Fig. 1. Boundary conditions and grid system for NACA0018 airfoil.

from the airfoil in a uniform stream. To apply Lighthill–Curle's equation to the moving sources interacting with airfoil boundary, we obtain Curle's formula (1955) for the limiting case of stationary airfoil surface $S$:

$$p'(\underline{x},t) = \frac{1}{4\pi}\frac{\partial^2}{\partial x_i \partial x_j}\int_V \frac{Q_{ij}(\underline{y}, t-\frac{r}{c_0})}{r}\mathrm{d}V(\underline{y}) - \frac{1}{4\pi}\frac{\partial}{\partial x_i}\int_S \frac{F_i(\underline{y}, t-\frac{r}{c_0})}{r}\mathrm{d}S(\underline{y}) \quad (15)$$

where $Q_{ij}$ $(= \rho\overline{u_i u_j} - \mu(\partial\bar{u}_i/\partial x_j + \partial\bar{u}_j/\partial x_i))$ is the Lighthill stress tensor, $F_i$ is a fluctuating force density field, and $r$ is the distance from the point source at $\underline{y}$ to a field point $\underline{x}$. For a continuous distribution of fluctuating stress ($Q_{ij}$) and force field of density ($F_i$) the sound field is given by the sum of a volume integral over the fluid and a surface integral over the region of flow containing the force field. The first term in Eq. (15) denotes the far-field acoustic pressure by quadrupole sources in the free-space fluid medium. The second term explains the effects of fluctuating forces over the airfoil including the pressures induced by the quadrupole sources near the trailing edge. If the space derivative is evaluated and the near field terms are neglected ($k_0 r \gg 1$), Eq. (15) reduces to

$$p'(\underline{x},t) \approx \frac{1}{4\pi c_0^2}\int_V \frac{(x_i-y_i)(x_j-y_j)}{r^3}\left[\frac{\partial^2 T_{ij}}{\partial t^2}\right]\mathrm{d}V(\underline{y}) - \frac{1}{4\pi c_0}\int_S \frac{x_i-y_i}{r^2}\left[\frac{\partial F_i}{\partial t}\right]\mathrm{d}S(\underline{y}) \quad (16)$$

The square brackets denote evaluation at the retarded time $(t - |\underline{x}-\underline{y}|/c_0)$ as in Eq. (16).

A fourth-order polynomial regression was applied to find the time derivatives of the surface force densities and Lighthill stress tensors, which reached the statistical steady states, at each retarded time by using non-dimensional time interval $(c_0 \cdot \Delta t/r)$ of $6.8\times10^{-5}$. Based on the assumption of the incoherent dominant sources (more discussion will follow), the total noise spectrum was computed by using all components of Lighthill tensors and forces acting on the surface with the implication of acoustic non-compactness in the spanwise direction. The previous research (Wang and Moin, 2000) dealt with two extreme cases: the case of a computational box size greater than coherence length and the case of a coherent source along the entire span.

Table 1
Comparison of separation points by experiment and computation for 3°, 6°, and 9° attack angles of NACA0018 airfoil

| Attack angle in degree | Surface type | Experiment ($x_1$/CL) | Computation ($x_1$/CL) |
|---|---|---|---|
| 3° | P.S. | 0.311 | 0.36 |
| | S.S. | 0.074 | 0.12 |
| 6° | P.S. | 0.407 | 0.46 |
| | S.S. | −0.096 | −0.08 |
| 9° | P.S. | 0.533 | 0.54 |
| | S.S. | −0.17 | −0.13 |

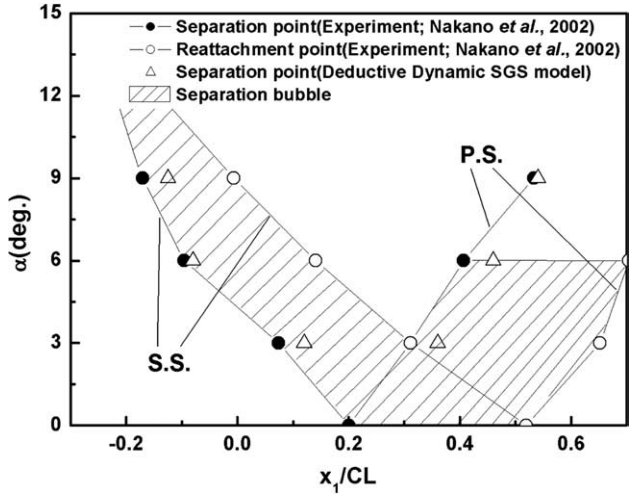


Fig. 2. Movements of the separation/reattachment lines according to the change of attack angle of NACA0018 airfoil.

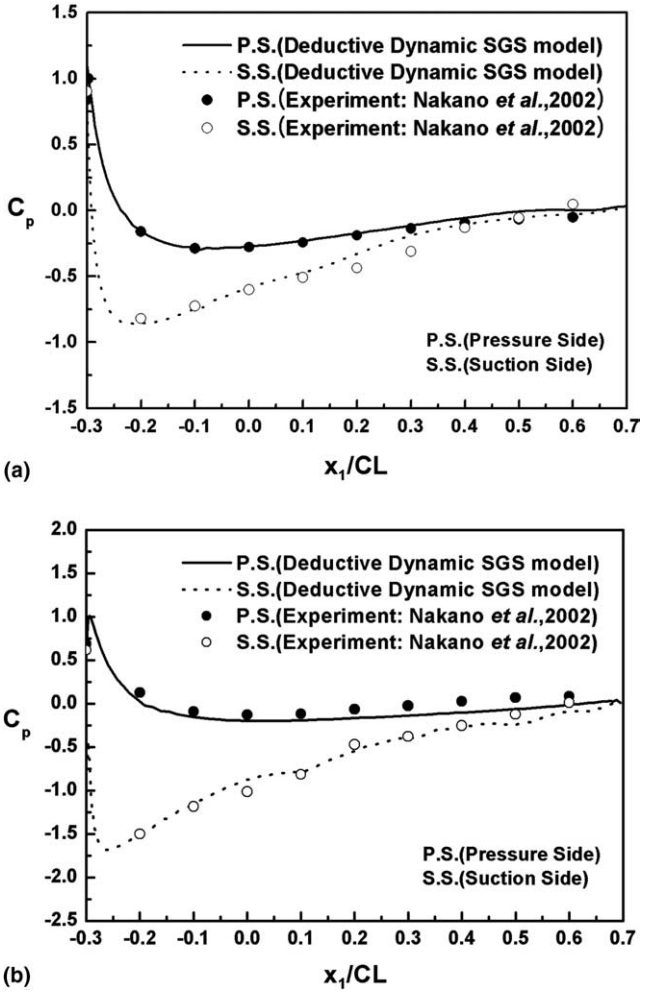


Fig. 3. Pressure coefficients for NACA0018 airfoil at angles of attack (a) $\alpha = 3°$ and (b) $\alpha = 6°$ ($Re_{CL} = 1.6\times10^5$).

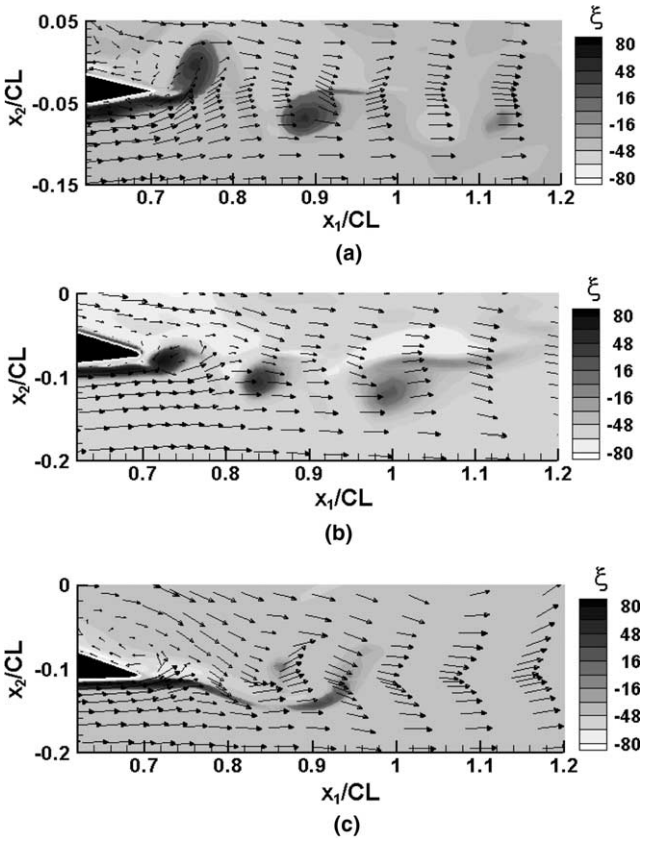


Fig. 4. Computed instantaneous vorticity fields around TE of airfoil at angles of attack (a) $\alpha = 3°$, (b) $\alpha = 6°$ and (c) $\alpha = 9°$.

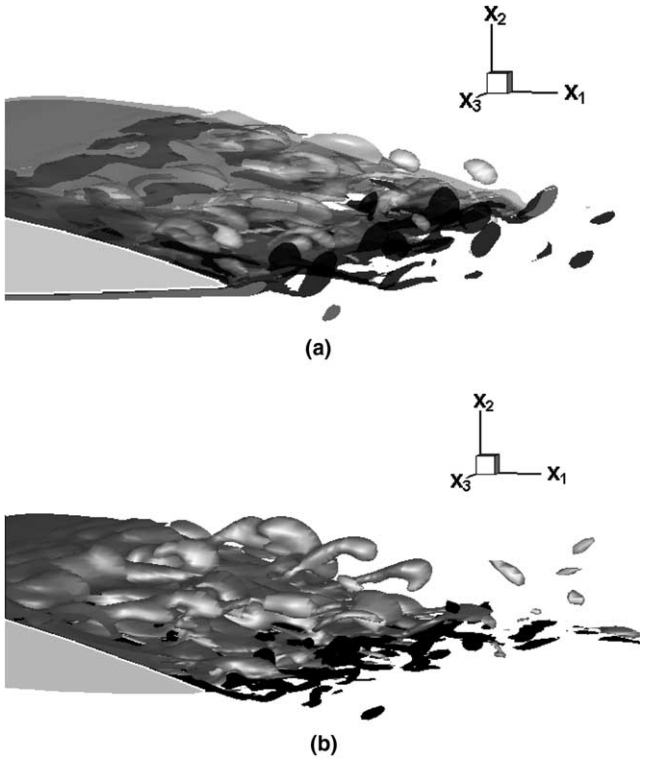


Fig. 5. Computed instantaneous iso-surfaces of the second invariant of the vorticity fields ($Q = \pm 10$) around TE on airfoil at angles of attack (a) $\alpha = 6°$ and (b) $\alpha = 9°$.

## 3. Results and discussion

### 3.1. Characteristics of flow over airfoil

As the attack angle increases, the flow velocity over the suction surface is decelerated and the pressure surface is accelerated, which results in an upstream movement of the separation and reattachment points on the suction surface and their downstream movements on the pressure surface. In the meantime, the boundary layer over the suction side receives a constant deceleration after passing the reattachment point, so that a thicker boundary layer is expected near the trailing edge of the suction side. On the other hand, the velocity outside the boundary layer on the pressure side remains almost constant along the airfoil surface and the reattachment point approaches the trailing edge of the airfoil. The separated flow prevails downstream over the pressure side except for the trailing edge of the airfoil at small angle of attack by the experiment (Tomimatsu and Fujisawa, 2002). To provide the global picture of the flow around the NACA0018 airfoil, the separation/reat-

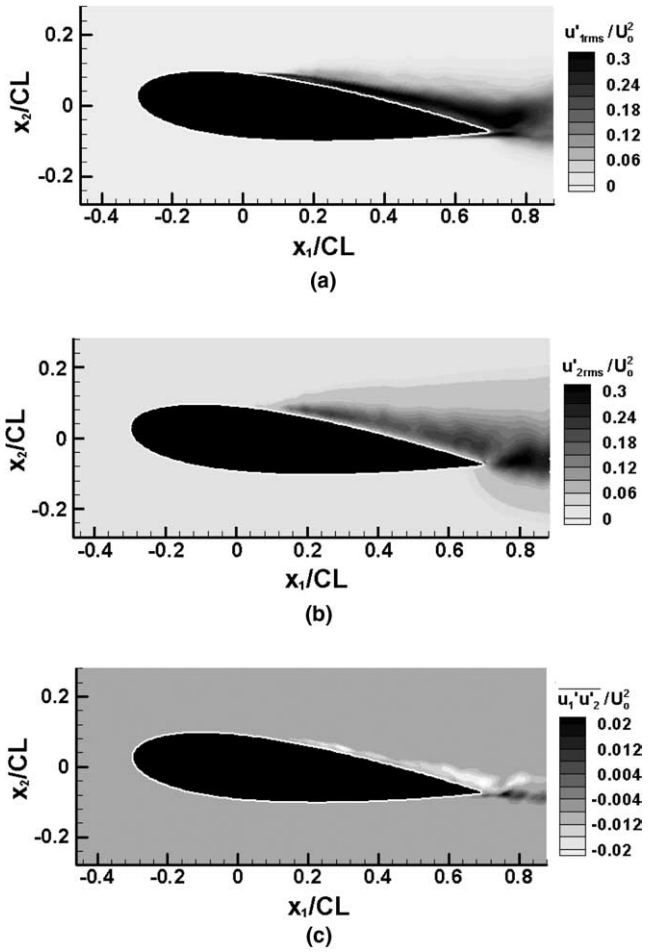


Fig. 6. Contours of turbulent stresses around airfoil at $\alpha = 6°$ by LES: (a) streamwise normal component, (b) transverse normal component and (c) Reynolds shear stress.

tachment lines according to the angle of attack are given in Fig. 2. In order to support the computational accuracy for the mean flow, the computed separation points are compared by using the Karman–Pohlhausen parameter $\Lambda = \frac{\delta^2}{\mu U_\infty}\left(\frac{dp}{dx}\right) = \frac{1}{2}\frac{\delta^2}{\nu}U_\infty\frac{dC_p}{dx}$ with the experimental ones, as shown in Table 1. Numerical prediction results in the movement of separation locations a little downstream for all cases because of no upstream turbulence imposed for the numerical case.

Fig. 3 shows distributions of mean surface pressure coefficients of the NACA0018 at attack angles of 3° and 6°, at which the discrete frequency noise is mostly produced by experiment. Although there are found some small discrepancies between experimental and numerical data, they are mostly due to the blockage effect of the test section and experimental scattering of the data. The experimental data was taken for the case of wall boundaries in the $x_2$- and $x_3$-directions while the open boundary was assumed in the computations in the $x_3$-direction to maintain the grid resolution in the spanwise $x_3$-direction. But it was confirmed experimentally that the wall boundary did not affect the discrete tone phenomena.

The examination of smoke pattern over the airfoil confirmed that the boundary layer downstream of the reattachment point over the suction side consists of a series of vortical structure and the separated laminar flow exists just upstream of the trailing edge on the pressure side of the airfoil (Nakano et al., 2002). In order to understand the flow phenomenon near the trailing edge of the airfoil, the instantaneous vorticity fields around the airfoil were reproduced. It is to be noted here that the vorticity is defined by $\zeta = CL/U_0(\partial u_2/\partial x_1 - \partial u_1/\partial x_2)$. It can be seen from Fig. 4 that the positive vortices are created from the pressure side and the negative vortices are produced from the suction side of the airfoil. The instantaneous vorticity fields in Fig. 4 were generated when the high amplitude events of pressure occurred very near the trailing edge of the pressure surface.

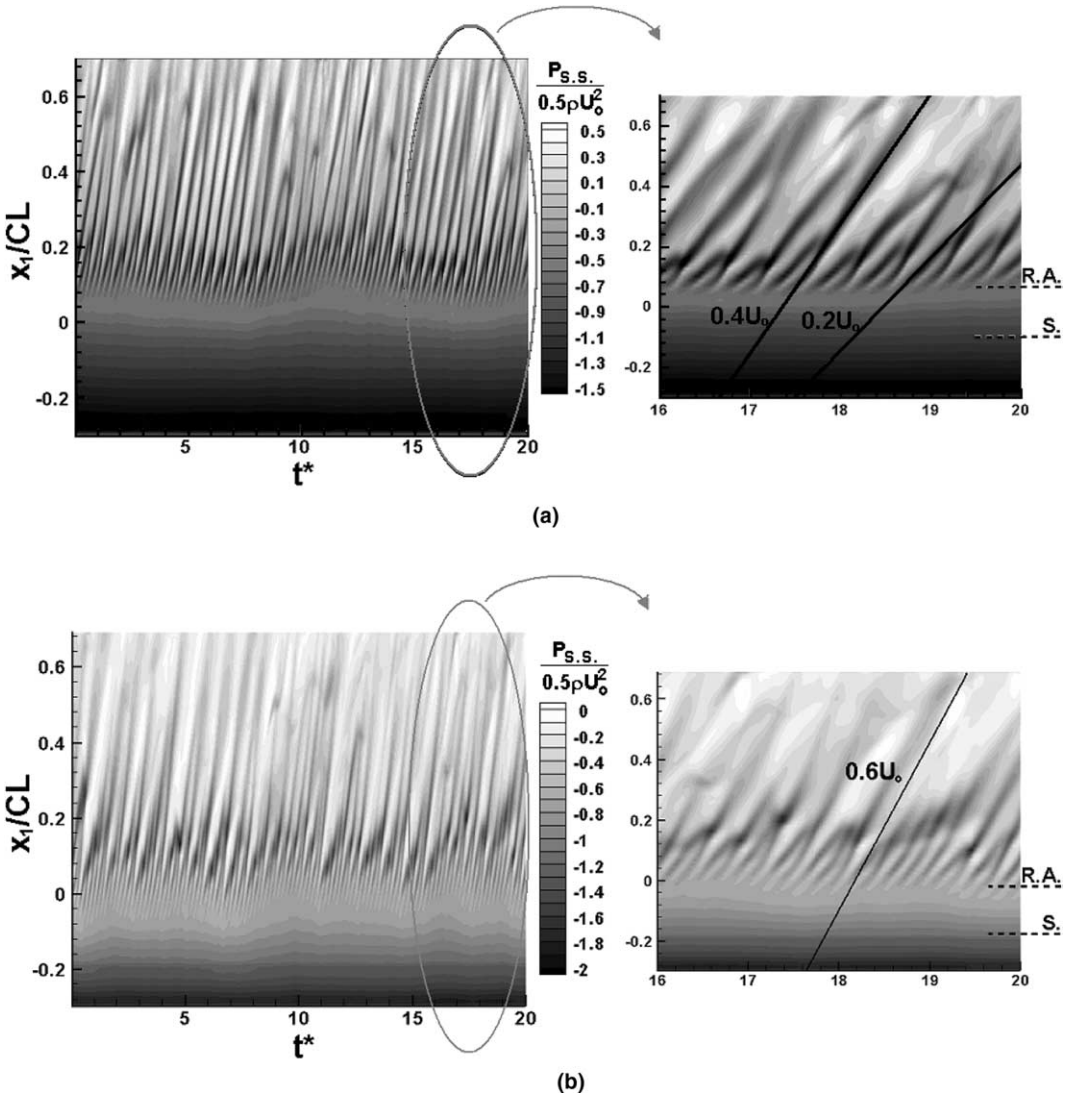


Fig. 7. Time history of fluctuating pressures on suction side of an airfoil centerline section at (a) $\alpha = 6°$ and (b) $\alpha = 9°$.

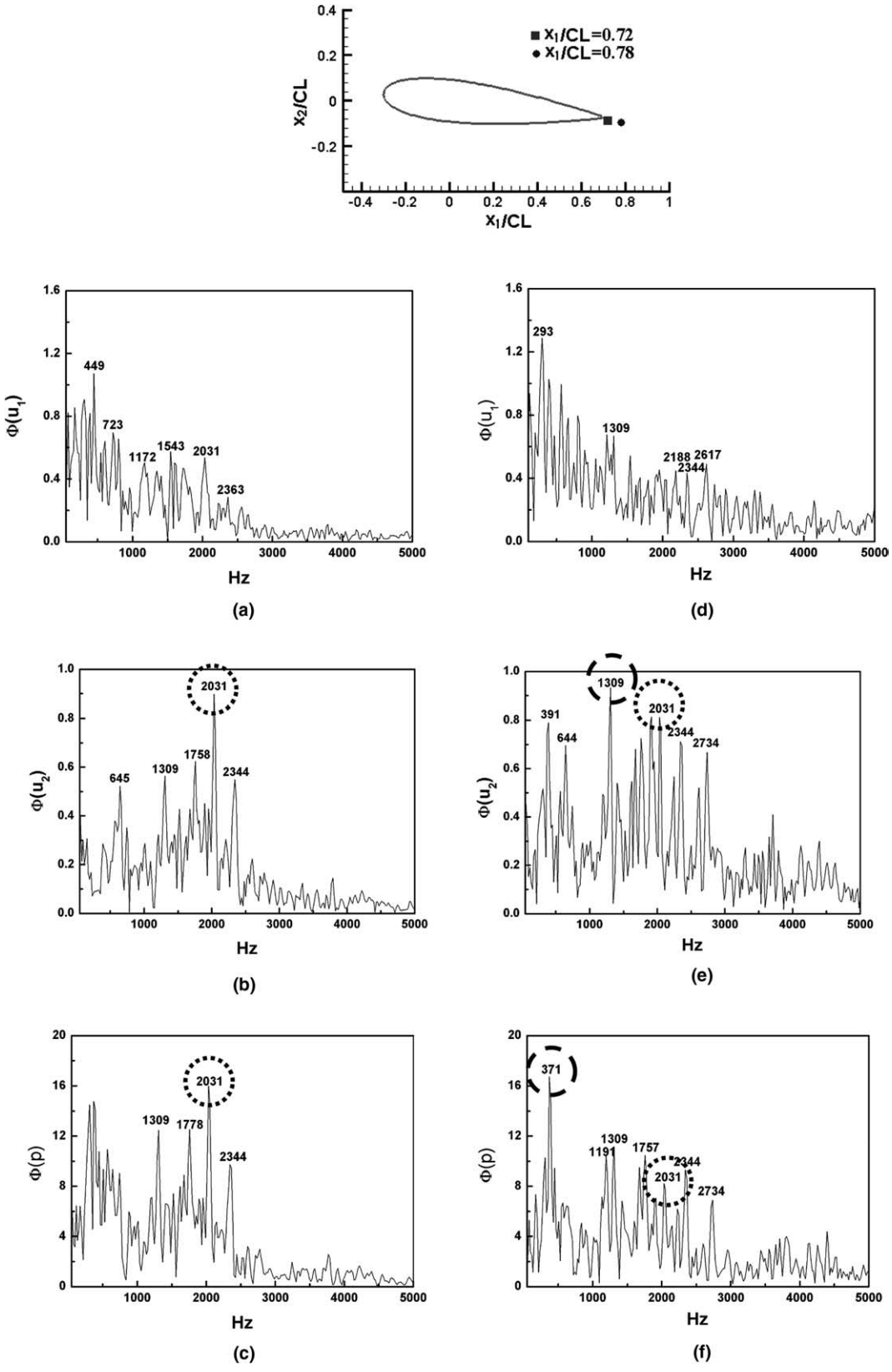


Fig. 8. Computed power spectra of streamwise and transverse components of velocity near TE at $\alpha = 6°$: (a) $\Phi(u_1)$, (b) $\Phi(u_2)$, (c) $\Phi(p)$ at $x_1/\mathrm{CL} = 0.72$, (d) $\Phi(u_1)$, (e) $\Phi(u_2)$ and (f) $\Phi(p)$ at $x_1/\mathrm{CL} = 0.78$.

The vorticity distribution over the pressure side at the attack angle of $\alpha = 3$–$6°$ is rather limited to the trailing edge of the airfoil, which suggests the production of vorticity by the reattachment of the separated boundary layer

near the trailing edge of the airfoil. The positive vorticities originated from the pressure side near the TE are observed to constitute the main structure of vortex shedding in the near-wake region for the cases of $\alpha = 3°$ and 6°, while the periodicity disappears for the case of $\alpha = 9°$.

To compare the unsteady structures on and around the airfoil for the cases of discrete and non-discrete sound generation, organized vortex structures on pressure and suction sides were identified by the iso-surfaces of the second invariant using $Q$-variable method (Jeong and Hussain, 1995), as shown in Fig. 5. While the vortex structures from the pressure side override the convecting vortices from the suction side at the attack angle of $\alpha = 6°$, the vortex structures from the pressure side are stretched in the downstream of the trailing edge by the irregular negative vortex structures from the suction surface at the attack angle of $\alpha = 9°$. The captured dominant structures are not found to be coherent in the spanwise domain of computational box.

The numerical simulations show two types of mode occurring near trailing edge, depending on how the flow near the trailing edge of the pressure side behaves. The positive vorticity is shed from the pressure side and the negative one is produced from the suction side. However, the former is usually much stronger than the latter in the magnitude. When the flow on the pressure side creates a positive vortex strong enough to penetrate into the shear layer originating from the suction side near trailing edge, the counter-rotating vortices are intermittently formed and upwardly convected. Otherwise, the vortex street moving downward is observed at all times.

To analyze time-averaged structures near the trailing edge for the most dominant case of discrete sound generation, the distributions of normal turbulent intensities of streamwise and transverse components, and normalized Reynolds stress around the TE are reproduced for the case of $\alpha = 6°$ in Fig. 6. It is interesting that the high turbulence intensities of the transverse component are more strongly generated behind the trailing edge and persists some distance downstream. Note that the transverse turbulence intensities are enhanced more strongly than the streamwise turbulence intensities, which suggests the interaction of shear layers developing on both surfaces of airfoil. The Reynolds shear stresses of positive values are found to grow from the reattachment point on the pressure side to the wake near TE where their maximum is observed.

To compare the unsteady structures on the suction side for cases of discrete and non-discrete sound generation, non-dimensional instantaneous pressures on suction sides of the two cases are plotted in terms of non-dimensional time ($t^* = t \cdot U_0/\mathrm{CL}$) in Fig. 7. The convection speeds of rolling vortices within the boundary layers of suction side are clearly identified by tracing their signatures of unsteady

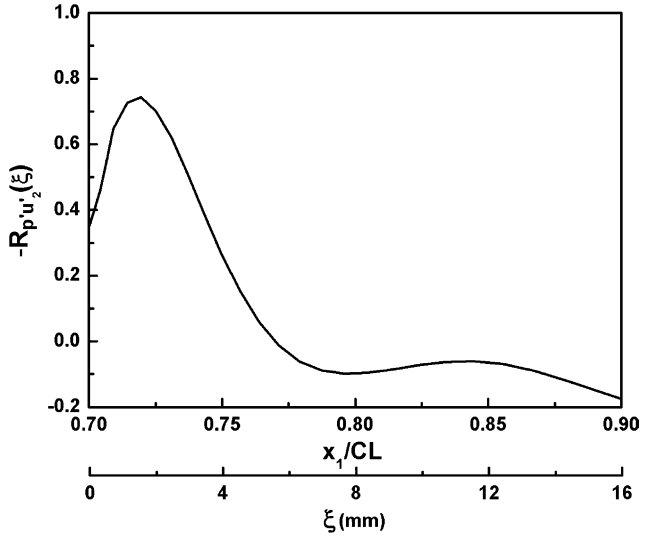


Fig. 9. Spatial cross-correlation $R_{p'u'_2}(\xi)$ of $p'$ at TE and $u'_2$ velocity component at a distance $\xi$ in the wake of NACA0018 airfoil at $\alpha = 6°$.

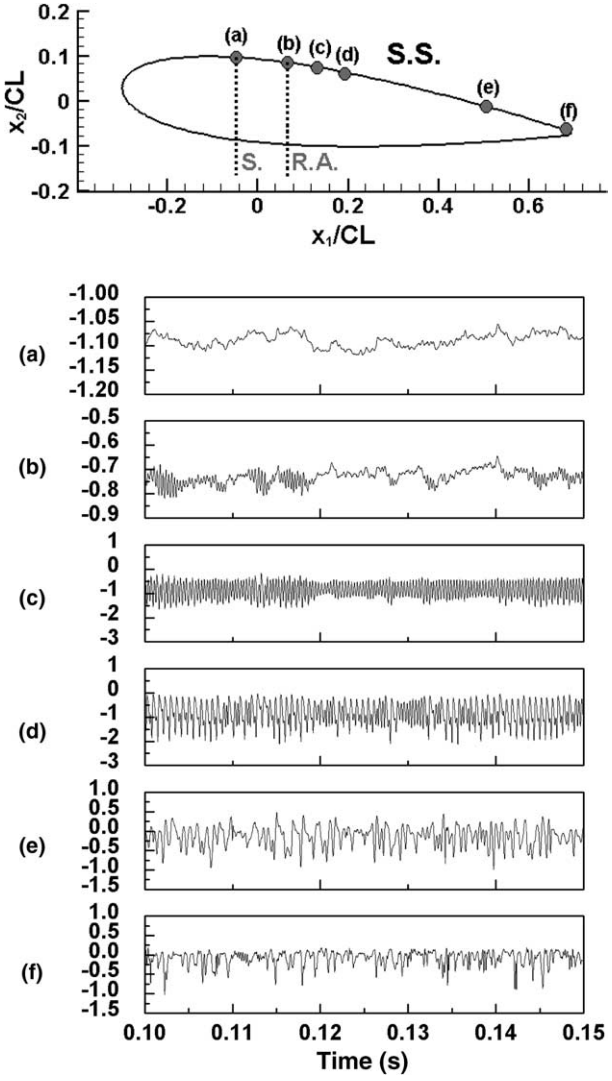


Fig. 10. Time signals of non-dimensional pressures at each $x_1/\mathrm{CL}$ value of suction side of NACA0018 blade at $\alpha = 6°$: (a) $x_1/\mathrm{CL} = -0.06$, (b) $x_1/\mathrm{CL} = 0.07$, (c) $x_1/\mathrm{CL} = 0.14$, (d) $x_1/\mathrm{CL} = 0.21$, (e) $x_1/\mathrm{CL} = 0.53$ and (f) $x_1/\mathrm{CL} = 0.69$.

events of pressures in the time domain, resulting in $0.4U_0$ and $0.6U_0$ except near the TE for the cases of $\alpha = 6°$ and 9°, respectively. The case of $\alpha = 6°$ shows two different modes of convection speed, which takes the value of $0.2U_0$ in $0.05 \leqslant x_1/\mathrm{CL} < 0.2$ intermittently and the stationary value of $0.4U_0$ downstream elsewhere. The convection speeds for the case of $\alpha = 6°$ seem to be more affected by the blocking motion of positive vortices from the pressure side near the TE than those for the case of as $\alpha = 9°$, shown in Fig. 4(a). Their motions are not related to the tonal noise generation.

It is also to be noted that the frequency of vortex formation at the trailing edge of the airfoil agreed closely with that of the discrete frequency noise measured in the experiment. In order to identify the frequency characteristics of vortex shedding, the frequency spectra of streamwise and cross-components of unsteady velocities downstream of the trailing edge are compared for $x_1/\mathrm{CL} = 0.72$ and 0.78. It is observed that the frequency of 2.03 kHz corresponds to the shedding frequency and the fluctuating cross-component of $u_2'$ is more pronounced at the shedding frequency as shown in Fig. 8. The quadrupole source near the TE usually generates much stronger blade-dipole sound than itself. To evaluate the contribution of the transverse component $u_2'$ to the fluctuating pressure near the TE, the spatial cross-correlation $R_{p'u_2'}(\xi)$ is computed as shown in Fig. 9. Based on the cross-correlation $R_{p'u_2'}(\xi)$, we may state that the structures near $x_1/\mathrm{CL} = 0.78$ are considered to contribute lesser to the total blade-dipole sound than the structures near $x_1/\mathrm{CL} = 0.72$ at the discrete frequency of 6° attack angle in Fig. 14(b).

To identify the unsteady pressure events occurring in the boundary layer of the airfoil, the time–frequency characteristics of events are analyzed by using the Choi–Williams

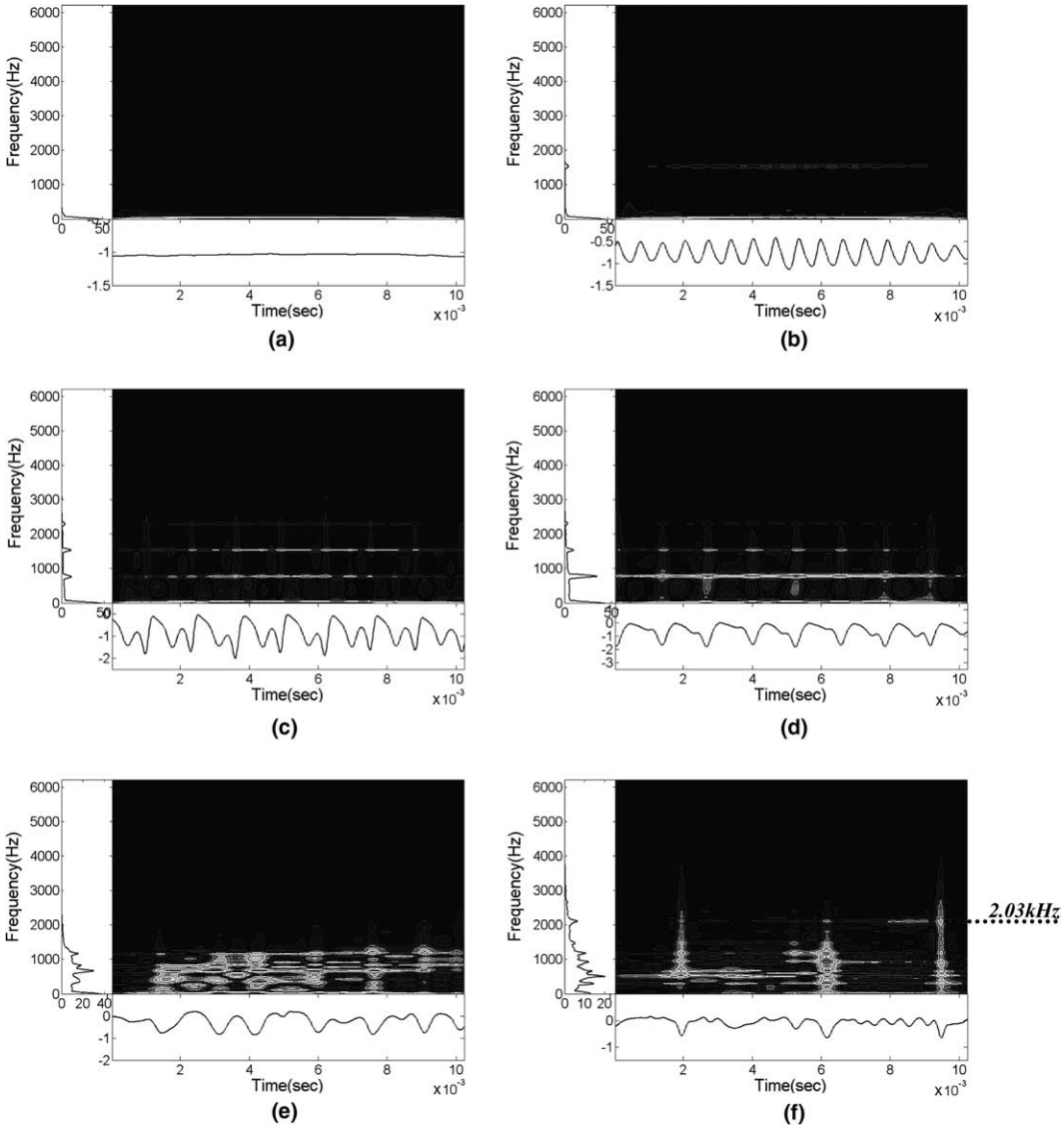


Fig. 11. Time–frequency analysis of fluctuating pressures on suction side at each $x_1/\mathrm{CL}$ of NACA0018 blade at $\alpha = 6°$ by Choi–Williams distribution method: (a) $x_1/\mathrm{CL} = -0.06$, (b) $x_1/\mathrm{CL} = 0.07$, (c) $x_1/\mathrm{CL} = 0.14$, (d) $x_1/\mathrm{CL} = 0.21$, (e) $x_1/\mathrm{CL} = 0.53$ and (f) $x_1/\mathrm{CL} = 0.69$.

kernel function in Wigner–Ville distribution method. The large-amplitude pressure events occurring in the separated boundary layer over an axisymmetric body were effectively analyzed using the Choi–Williams distribution method by Lee et al. (2000). The bilinear time and frequency transformation of time-varying raw signals can be written as

$$S(t,f)=\int_{-\infty}^{\infty}\Phi(u-t,\tau)x\left(u+\frac{\tau}{2}\right)x^{*}\left(u-\frac{\tau}{2}\right)\mathrm{e}^{-\mathrm{j}2\pi f\tau}\,\mathrm{d}u\,\mathrm{d}\tau \tag{17}$$

where $\Phi(t,\tau)$ is a smoothing kernel function. In the Choi–Williams distribution method, an exponential kernel is used to provide an adequate window having enough frequency resolutions for large-amplitude events as given in Eq. (17) (Choi and Williams, 1989).

$$W(t,f)=\int_{\tau}\mathrm{e}^{-2\pi f\tau}\int_{u}\frac{1}{2\tau}\times\sqrt{\frac{v}{\pi}}\mathrm{e}^{-\mathrm{j}2\pi\left(f\tau+v\frac{(u-t)^{2}}{4\tau^{4}}\right)}x\left(u+\frac{\tau}{2}\right)x^{*}\left(u-\frac{\tau}{2}\right)\mathrm{e}^{-\mathrm{j}2\pi f\tau}\,\mathrm{d}u\,\mathrm{d}\tau \tag{18}$$

where $v$ ($v>0$) is a scaling parameter and kernel shape coefficient. The event detection algorithm has the frequency resolution of 1024 for large amplitude or quasi-periodic pressure at each time.

In Figs. 10 and 12, the time signals of simulated unsteady pressures at the specified locations of $x_1/\mathrm{CL}$ are given for suction and pressure surfaces, respectively. The slowly fluctuating and the very regular disturbances are observed at the separation point (a) and the reattachment point (c) on suction side, respectively. But the computed real-time pressure signals on the pressure surface does not allow the clear definition of reattachment point near the trailing edge in Fig. 12.

In an effort to supplement the pressure signals in time and assess the contribution of each source in the boundary layer to the discrete noise component, the event detection method by time–frequency representation was applied to the fluctuating pressure signals at the specified locations (separation, reattachment, etc.) in the boundary layer. The pressure signatures on the suction surface, as shown in Fig. 11, reveal the events consisting of a quasi-periodic motion of 750 Hz and its harmonics by rolling vortices in the attached boundary layer. On the other hand, the event patterns on the pressure surface of the airfoil in Fig. 13 may be grouped into a low-frequency stable region before separation point (b), a mid-frequency zone of growing instabilities in the separated bubble (c and d), and a region of large-amplitude pressure events near TE (e and f). The main events around 2.03 kHz near TE, as shown in Fig. 13(f), are assumed to be mostly correlated with the shedding vortices of discrete sound. Hence, we may observe from this case that the discrete frequency noise can be created by the strong instability of 2.03 kHz after the reattachment of the separated laminar flow on the pressure side. The periodicity of negative vortices on the suction side near TE seems to be also affected by the positive vortices shed downstream of TE, as shown in Fig. 11(f).

### 3.2. Characteristics of aerodynamic noise

The instantaneous acoustic pressure signatures at a far-field point in the normal direction to the blade are obtained for the case of $\alpha=6°$ by solving Eq. (16) and separately given for the dipole and the quadrupole terms in Fig. 14(a). The sound spectrum by dipole sources in Fig. 14(b) indicates a primary discrete peak at a frequency of 2.03 kHz, the same as the one predicted by the Choi–Williams analysis, when the angle of attack is set to $\alpha=6°$ against the free-stream direction. This primary peak frequency corresponds to a Strouhal number $St$ ($=2f\cdot\delta/U_0$) $=0.15$, which compares closely with the experimental data of $St=0.16$ by

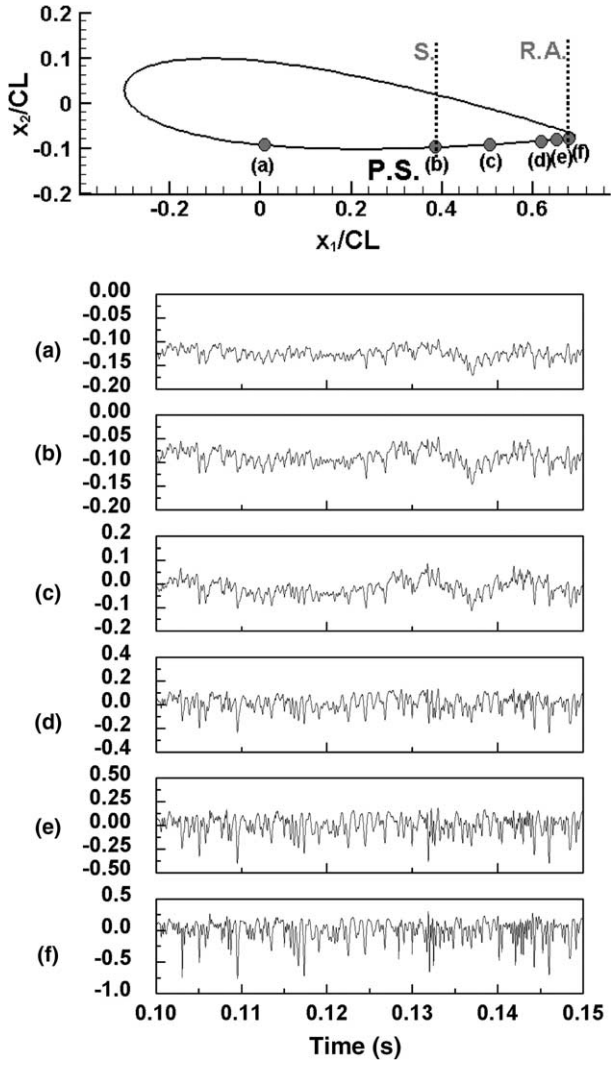


Fig. 12. Time signals of non-dimensional pressures at each $x_1/\mathrm{CL}$ value of pressure side of NACA0018 blade at $\alpha=6°$: (a) $x_1/\mathrm{CL}=0.03$, (b) $x_1/\mathrm{CL}=0.39$, (c) $x_1/\mathrm{CL}=0.53$, (d) $x_1/\mathrm{CL}=0.63$, (e) $x_1/\mathrm{CL}=0.67$ and (f) $x_1/\mathrm{CL}=0.69$.

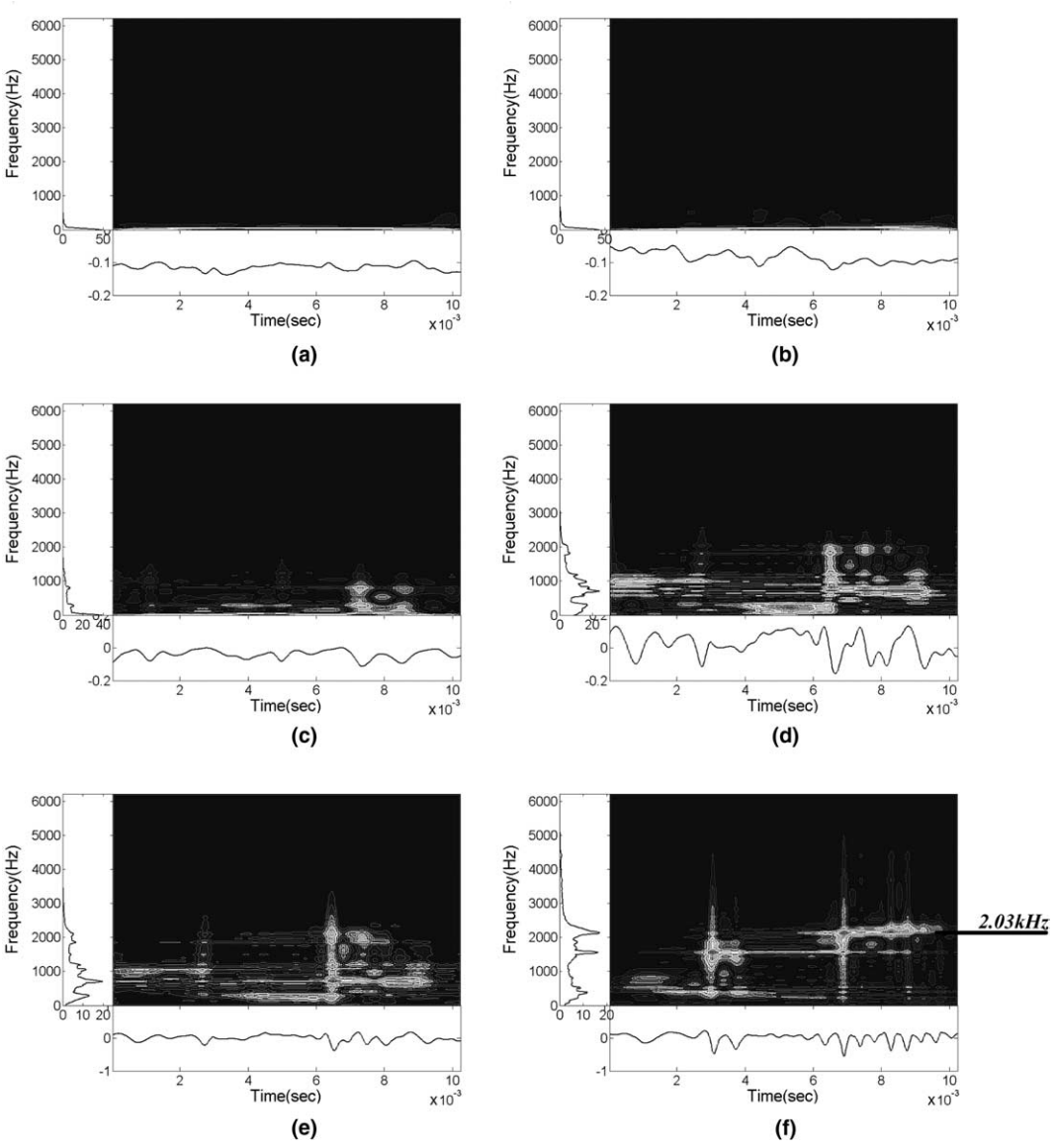


Fig. 13. Time–frequency analysis of fluctuating pressures on pressure side at each $x_1$/CL of NACA0018 blade at $\alpha = 6°$ by Choi–Williams distribution method: (a) $x_1/\mathrm{CL} = 0.03$, (b) $x_1/\mathrm{CL} = 0.39$, (c) $x_1/\mathrm{CL} = 0.53$, (d) $x_1/\mathrm{CL} = 0.63$, (e) $x_1/\mathrm{CL} = 0.67$ and (f) $x_1/\mathrm{CL} = 0.69$.

Nakano et al. (2002) ($\delta$: thickness of laminar boundary layer on the pressure side at the trailing edge).

As can be seen, the acoustic pressures by dipole sources have 2–3 order higher in the low-frequency range (<1 kHz) and 1–2 order higher in the high-frequency range (>1 kHz) except at the discrete frequency than the acoustic pressures by quadrupole sources, respectively. The magnitude ratio between the quadrupole sound and the induced dipole sound is known to depend strongly on CL/$\lambda$. While the numerical Curle's approach considers the separate contribution to the total sound, it is very difficult to realize each contribution in the experiment.

The aerodynamic noise observed in the present simulation is considered to be of the same kind due to the discrete tone noise. Far-field radiated sound from the blade was computed using the time-dependent flow field as described earlier, for the full range of radiation angles in 10° increments at 10 m ($R$) from the center of blade chord. Radiation angle is defined such that 0° is along the free-stream velocity vector $U_0$. Overall sound pressure level (OASPL) was calculated after averaging sound pressures obtained from more than 200 realizations, and normalized to the reference radius of 0.095 m for comparison.

The simulated OASPL's versus radiation angle by dipole and quadrupole sources are made in Fig. 14(c) for the incidence angle of 6°. The simulated result shows the maximum radiation along the normal direction to blade chord, stating that the vortex shedding near the trailing edge exhibits the characteristics of a dipole source. When the acoustic wavelength and the chord length are comparable, the dipole directivity by Curle's solution of the free-space acoustic Green's function is known to deviate from that by the sound-hard Green's function (Oberai et al., 2002). The discrete frequency of 2.03 kHz corresponding

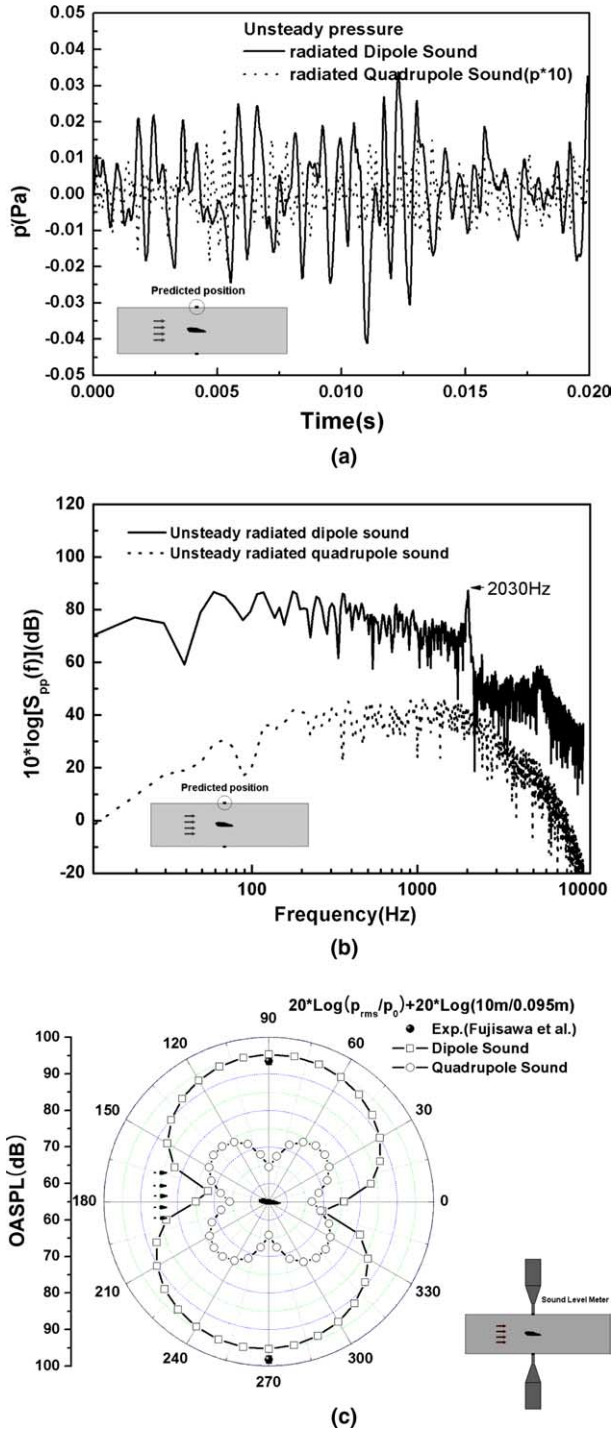


Fig. 14. Computed (a) instantaneous acoustic pressure signatures at a far-field, (b) auto-spectra of acoustic pressures shown in (a), (c) directivity patterns by dipole and quadrupole sources around NACA0018 airfoil at $\alpha = 6°$.

to CL/$\lambda \approx 1/2$ ($\lambda$: acoustic wave length) may belong to this category. Even though the simulated magnitude from the dipole sound is in agreement with the measured one at the radiation angle of 90° in the figure, the simulated overall directivity may deviate significantly from the measured one. The quadrupole sound is found to be much weaker than the dipole sound and has a butterfly pattern of radiation.

## 4. Conclusion

The flow mechanism of discrete frequency noise from a symmetrical airfoil in a uniform flow was studied by the numerical simulation. The numerical results show that the discrete frequency noise is observed when the airfoil is inclined at small angle of attack to the free stream.

The examination of the flow characteristics over the airfoil under the generation of noise indicates that the laminar separated flow is reattached over the airfoil surface near the trailing edge on the pressure side of the airfoil and the strong instability after the reattachment point affects positive vortices shed near the trailing edge. On the other hand, the turbulent boundary layer is formed over the suction side of the airfoil and the quasi-periodic behavior of negative vortex formation on the suction side is affected by the strength and the periodicity of positive vortices near the trailing edge. Therefore, the flow reattachment near the trailing edge of pressure side is responsible for producing large positive vorticities in the wake of the airfoil and thereby generating discrete sound.

A hybrid method using acoustic analogy of Curle's formula of a free-space acoustic Green's function was employed to compute the far-field sound spectrum and the directivity pattern of OASPL's from the airfoil in the uniform stream. The sound spectrum by the dipole-source assumption indicates the primary discrete peak at the frequency of 2.03 kHz corresponding to the Strouhal number $St$ ($=2f\cdot\delta/U_0$) of 0.15 when the angle of attack is set to $\alpha = 6°$. The frequency of the vortex formation is found to be consistent with that of the discrete frequency noise. However, this result does not include the scattering effect by the finite airfoil at high frequencies, which is not a primary issue for this case.

## Acknowledgments

This research was supported by University IT Research Center Project under the supervision of IITA. The authors express thanks to Prof. Culick, F.E.C. at California Institute of Technology and Dr. Runchal, A.K. at ACRi for their help on this research.

## Appendix A

The generalized Leonard stress tensor $L_{ij}$ is defined as

$$L_{ij} = \widehat{\bar{u}_i\bar{u}_j} - \hat{\bar{u}}_i\hat{\bar{u}}_j \tag{A.1}$$

Applying Taylor series expansion to $\widehat{\bar{u}_i\bar{u}_j}$,

$$\bar{u}_i\bar{u}_j = \bar{u}_i\bar{u}_j + \frac{\Delta_T^2}{24}\frac{\partial^2(\bar{u}_i\bar{u}_j)}{\partial x_l^2} + \frac{1}{2}\widehat{\left(\frac{\Delta_T^2}{24}\right)^2}\frac{\partial^2}{\partial x_l^2}\frac{\partial^2}{\partial x_m^2}\bar{u}_i\bar{u}_j + O(\Delta_T^6) \tag{A.2}$$

Expanding the second derivative $\partial^2(\bar{u}_i\bar{u}_j)/\partial^2 x_l$ as in (A.3), and substituting (A.3) into (A.2) gives (A.4)

$$\frac{\partial^2(\bar{u}_i\bar{u}_j)}{\partial x_l^2} = \bar{u}_i\frac{\partial^2\bar{u}_j}{\partial x_l^2} + 2\frac{\partial\bar{u}_i}{\partial x_l}\frac{\partial\bar{u}_j}{\partial x_l} + \bar{u}_j\frac{\partial^2\bar{u}_i}{\partial x_l^2} \tag{A.3}$$

$$\widehat{\bar{u}_i\bar{u}_j} = \bar{u}_i\bar{u}_j + \frac{\Delta_T^2}{24}\left(\bar{u}_i\frac{\partial^2\bar{u}_j}{\partial x_l^2} + \bar{u}_j\frac{\partial^2\bar{u}_i}{\partial x_m^2}\right) + \frac{\Delta_T^2}{12}\frac{\partial\bar{u}_i}{\partial x_l}\frac{\partial\bar{u}_j}{\partial x_l} + \frac{\Delta_T^4}{1152}\frac{\partial^2}{\partial^2 x_l}\frac{\partial^2}{\partial^2 x_m}\bar{u}_i\bar{u}_j + O(\Delta_T^6) \tag{A.4}$$

Applying Taylor series expansions to $\hat{\bar{u}}_i$ and $\hat{\bar{u}}_j$ as in (A.5), and making the product of them gives (A.6)

$$\hat{\bar{u}}_i = \left[\bar{u}_i + \frac{\Delta_T^2}{24}\frac{\partial^2\bar{u}_i}{\partial x_l^2} + \frac{1}{2}\left(\frac{\Delta_T^2}{24}\right)^2\frac{\partial^2}{\partial x_l^2}\frac{\partial^2}{\partial x_m^2}\bar{u}_i + O(\Delta_T^6)\right] \tag{A.5}$$

$$\hat{\bar{u}}_i\hat{\bar{u}}_j = \bar{u}_i\bar{u}_j + \frac{\Delta_T^2}{24}\left(\bar{u}_i\frac{\partial^2\bar{u}_j}{\partial x_l^2} + \bar{u}_j\frac{\partial^2\bar{u}_i}{\partial x_m^2}\right) + \left(\frac{\Delta_T^2}{24}\right)^2\frac{\partial^2\bar{u}_i}{\partial x_m^2}\frac{\partial^2\bar{u}_j}{\partial x_l^2} + \frac{\Delta_T^4}{1152}\left(\bar{u}_i\frac{\partial^2}{\partial x_l^2}\frac{\partial^2}{\partial x_m^2}\bar{u}_j + \bar{u}_j\frac{\partial^2}{\partial x_l^2}\frac{\partial^2}{\partial x_m^2}\bar{u}_i\right) + O(\Delta_T^6) \tag{A.6}$$

Combining in (A.4) and (A.6) to get the generalized Leonard stress tensor gives

$$L_{ij} = \frac{\Delta_T^2}{12}\left(\frac{\partial\bar{u}_i}{\partial x_l}\frac{\partial\bar{u}_j}{\partial x_l}\right) - \left(\frac{\Delta_T^2}{24}\right)^2\frac{\partial^2\bar{u}_i}{\partial x_m^2}\frac{\partial^2\bar{u}_j}{\partial x_l^2} + \frac{\Delta_T^4}{1152}\left[\frac{\partial^2}{\partial x_l^2}\frac{\partial^2}{\partial x_m^2}\bar{u}_i\bar{u}_j - \left(\bar{u}_i\frac{\partial^2}{\partial x_l^2}\frac{\partial^2}{\partial x_m^2}\bar{u}_j + \bar{u}_j\frac{\partial^2}{\partial x_l^2}\frac{\partial^2}{\partial x_m^2}\bar{u}_i\right)\right] + O(\Delta_T^6) \tag{A.7}$$

The generalized $M_{ij}$ is defined as

$$M_{ij} = \left(\Delta_{GT}^2\left|\hat{\bar{S}}\right|\hat{\bar{S}}_{ij} - \Delta_G^2\widehat{|\bar{S}|\bar{S}_{ij}}\right) \tag{A.8}$$

Applying Taylor series expansion to $\Delta_G^2\widehat{|\bar{S}|\bar{S}_{ij}}$

$$\Delta_G^2\widehat{|\bar{S}|\bar{S}_{ij}} = \Delta_G^2\overline{|S|}\overline{S}_{ij} + \frac{\Delta_T^2}{24}\frac{\partial^2\left(\Delta_G^2\overline{|S|}\overline{S}_{ij}\right)}{\partial x_l^2} + \frac{\Delta_T^4}{1152}\left(\frac{\partial^2\left(\Delta_G^2\overline{|S|}\overline{S}_{ij}\right)}{\partial x_l^2}\right)^2 + O(\Delta_T^6) \tag{A.9}$$

Expanding the second derivative term gives

$$\frac{\partial^2\left(\Delta_G^2\overline{|S|}\overline{S}_{ij}\right)}{\partial x_l^2} = 2\Delta_G^2\frac{\partial\overline{|S|}}{\partial x_l}\frac{\partial\overline{S}_{ij}}{\partial x_l} + \Delta_G^2\overline{|S|}\frac{\partial^2\overline{S}_{ij}}{\partial x_l^2} + \Delta_G^2\overline{S}_{ij}\frac{\partial^2\overline{|S|}}{\partial x_m^2} \tag{A.10}$$

$$\Delta_G^2\widehat{|\bar{S}|\bar{S}_{ij}} = \Delta_G^2\overline{|S|}\overline{S}_{ij} + \frac{\Delta_T^2}{24}\left(\Delta_G^2\overline{|S|}\frac{\partial^2\overline{S}_{ij}}{\partial x_l^2} + \Delta_G^2\overline{S}_{ij}\frac{\partial^2\overline{|S|}}{\partial x_l^2} + 2\Delta_G^2\frac{\partial\overline{|S|}}{\partial x_l}\frac{\partial\overline{S}_{ij}}{\partial x_l}\right) + \frac{\Delta_T^4}{1152}\frac{\partial^2}{\partial x_l^2}\frac{\partial^2}{\partial x_m^2}\Delta_G^2\overline{|S|}\overline{S}_{ij} + O(\Delta_T^6) \tag{A.11}$$

Applying Taylor series expansion to $\Delta_{GT}^2\left|\hat{\bar{S}}\right|\hat{\bar{S}}_{ij}$

$$\Delta_{GT}^2\left|\hat{\bar{S}}\right|\hat{\bar{S}}_{ij} = \Delta_{GT}^2\overline{|S|}\overline{S}_{ij} + \Delta_{GT}^2\frac{\Delta_T^2}{24}\left(\overline{|S|}\frac{\partial^2\overline{S}_{ij}}{\partial x_l^2} + \overline{S}_{ij}\frac{\partial^2\overline{|S|}}{\partial x_l^2}\right) + \Delta_{GT}^2\left(\frac{\Delta_T^2}{24}\right)^2\frac{\partial^2\overline{|S|}}{\partial x_l^2}\frac{\partial^2\overline{S}_{ij}}{\partial x_m^2} + \Delta_{GT}^2\frac{\Delta_T^4}{1152}\left(\overline{|S|}\frac{\partial^2}{\partial x_l^2}\frac{\partial^2}{\partial x_m^2}\overline{S}_{ij} + \overline{S}_{ij}\frac{\partial^2}{\partial x_l^2}\frac{\partial^2}{\partial x_m^2}\overline{|S|}\right) + O(\Delta_T^6) \tag{A.12}$$

Substituting (A.11) and (A.12) into (A.8) gives the generalized $M_{ij}$ as in (A.13):

$$M_{ij} = \left(\Delta_{GT}^2 - \Delta_G^2\right)\overline{|S|}\overline{S}_{ij} + \frac{\Delta_T^2\cdot\left(\Delta_{GT}^2 - \Delta_G^2\right)}{24}\times\left(\overline{|S|}\frac{\partial^2\overline{S}_{ij}}{\partial x_l^2} + \overline{S}_{ij}\frac{\partial^2\overline{|S|}}{\partial x_m^2}\right) + \Delta_{GT}^2\left(\frac{\Delta_T^2}{24}\right)^2\frac{\partial^2\overline{|S|}}{\partial x_l^2}\frac{\partial^2\overline{S}_{ij}}{\partial x_m^2} - \frac{\Delta_G^2\cdot\Delta_T^2}{12}\frac{\partial\overline{|S|}}{\partial x_l}\frac{\partial\overline{S}_{ij}}{\partial x_l} + \frac{\Delta_T^4}{1152}\left[\Delta_{GT}^2\overline{|S|}\frac{\partial^2}{\partial x_l^2}\frac{\partial^2}{\partial x_m^2}\overline{S}_{ij} + \Delta_{GT}^2\overline{S}_{ij}\frac{\partial^2}{\partial x_l^2}\frac{\partial^2}{\partial x_m^2}\overline{|S|} - \frac{\partial^2}{\partial x_l^2}\frac{\partial^2}{\partial x_m^2}\Delta_G^2\overline{|S|}\overline{S}_{ij}\right] + O(\Delta_T^6) \tag{A.13}$$

## References


Akishita, S., 1986. Tone-like noise from an isolated two dimensional airfoil. AIAA Paper 86-1947.

Choi, H.I., Williams, W., 1989. Improved time–frequency representation of multiple component signals using an exponential kernel. IEEE Transactions 37, 862–971.

Curle, N., 1955. Influence of solid boundaries upon aerodynamic sound. Proceedings of the Royal Society (London) Series A 231, 506–514.

Dawes, W.N., 1986. Development of a 3D Navier–Stokes solver for application to all types of turbomachinery. ASME Paper No. 86-GT-70.

Denton, J.D., 1986. The use of a distributed body force to simulate viscous flow in 3D flow calculation. ASME Paper No. 86-GT-144.

Ffowcs Williams, J.E., Hall, L.H., 1970. Aerodynamic sound generated by turbulent flow in the vicinity of a scattering half plane. Journal of Fluid Mechanics 40, 657–670.

Fujisawa, N., Shibuya, S., Nashimoto, A., Takano, T., 2001. Aerodynamic noise and flow visualization around two-dimensional airfoil. Journal of Visualization Society of Japan 21, 123–129 (in Japanese).

Germano, M., 1992. Turbulence: the filtering approach. Journal of Fluid Mechanics 238, 325–336.

Germano, M., Piomelli, U., Moin, P., Cabot, W.H., 1991. A dynamic subgrid-scale eddy viscosity model. Physics of Fluids (A) 3, 1760–1765.

Hah, C., 1987. Calculation of three-dimensional viscous flows in turbomachinery with an implicit relaxation method. AIAA Journal of Propulsion and Power 3, 415–422.

Hayashi, H., Kodama, Y., Fukano, Y., Ikeda, M., 1995. Relationship between wake vortex formation and discrete frequency noise in NACA blades. Transaction of Japan Society of Mechanical Engineers 61 (B), 2109–2114 (in Japanese).

Hayder, M.E., Turkel, E., 1995. Non-reflecting boundary conditions for jet flow computations. AIAA Journal 33 (12), 2264–2270.

Howe, M.E., 2001. Edge-source acoustic Green's function for an airfoil of arbitrary chord, with application to trailing-edge noise. Quarterly Journal of Mechanics and Applied Mathematics 54 (1), 139–155.

Jeong, J.H., Hussain, F., 1995. On the identification of a vortex. Journal of Fluid Mechanics 285, 69–94.

Lee, S., Kim, H.-J., Kwon, O.-S., Lee, S.K., 2000. Wall pressure fluctuations and radiated sound from turbulent boundary layer on an axisymmetric body. Acoustical Society America ARLO 1 (1), 7–12.

Lee, S., Kim, H.-J., Runchal, A., 2004a. Large-eddy simulation of unsteady flows in turbomachinery. Journal of Power and Energy (A) 218, 463–475.

Lee, S., Kim, H.-J., Kim, J.-H., Song, S.-J., 2004b. Computation of turbulent flows and radiated sound from axial compressor cascade. KSME International Journal 18 (2), 272–285.

Leonard, B.P., 1979. A stable and accurate convective modeling procedure based on quadratic upstream interpolation. Computer Methods in Applied and Mechanical Engineering 19, 59–98.

Lilly, D.K., 1992. A Proposed modification of the Germano subgrid-scale closure method. Physics of Fluids (A) 4, 633–635.

Nakano, T., Kim, H.-J., Lee, S., Fujisawa, N., Takagi, Y., 2002, A study on discrete frequency noise from a symmetrical airfoil in a uniform flow. In: 5th JSME-KSME Fluids Engineering Conference, OS6-2-4, November 17–21, Nagoya, Japan.

Oberai, A.A., Roknaldin, F., Hughes, T.J.R., 2000. Computational procedures for determining structural-acoustic response due to hydrodynamic sources. Computer Methods in Applied Mechanics and Engineering 190, 345–361.

Oberai, A.A., Roknaldin, F., Hughes, T.J.R., 2002. Computation of trailing-edge noise due to turbulent flow over an airfoil. AIAA Journal 40 (11), 2206–2216.

Paterson, R.W., Vogt, P.G., Fink, M.R., Munch, C.L., 1973. Vortex noise of isolated airfoils. Journal of Aircraft 10, 296–302.

Runchal, A.K., Bhatia, S.K., 1993. ASME benchmark study: ANSWER predictions for backward facing step and lid-driven cubical cavity. ASME FED 160, 43–54.

Smagorinsky, J., 1963. General circulation experiments with the primitive equations, Part I: the basic experiment. Monthly Weather Review 91, 99–164.

Saxer-Felici, H.M., Saxer, A.P., Inderbitzin, A., Gyarmathy, G., 2000. Numerical and experimental study of rotating stall in an axial compressor stage. AIAA Journal 38, 1132–1141.

Tam, C.K.W., 1974. Discrete tones of isolated airfoils. Journal of Acoustic Society of America 55, 1173–1177.

Tomimatsu, S., Fujisawa, N., 2002. Measurement of aerodynamic noise and unsteady flow field around a symmetrical airfoil. Journal of Visualization 5, 381–388.

Wang, M., Moin, P., 2000. Computation of trailing-edge flow and noise using large-eddy simulation. AIAA Journal 38 (12), 2201–2209.